

Cerro Catedral radar: improvement recipes and data quality analysis.

A. V. Magaldi*

5 Centro de Ciencias de la Atmósfera, Universidad Nacional Autónoma de México,
6 Mexico City, Mexico

* Corresponding author; email: adolflo.magaldi@atmosfera.unam.mx

10

Abstract

11 Weather radar quantitative precipitation estimation (QPE) is the usual tool to en-
12 sure a correct rainfall intensity measurement. This technique is wide used by forecasters
13 and hydrological models. The QPE requires the application of several quality control pro-
14 cedures to warranty an optimal radar performance. In particular, the identification and
15 suppression of spurious echoes due to the ground clutter provide a more accurate rain
16 field from the radar data. These spurious echoes are generated by the interaction of the
17 radar beam with several types of non-hydrometeorological targets. Usually, the Doppler
18 filter applied in the post-processing stage is a good tool to eliminate this type of spurious
19 echoes. However, many studies have shown that, in addition to this filter, a series of extra
20 algorithms are required in order to guarantee the elimination of this type of echoes.

21 Based on previous efforts to depict the non-precipitating echoes from radar data, a
22 methodology based on tree algorithms was applied over the Cerro Catedral radar data in
23 order to identify and remove the spurious echoes, correct the attenuation and perform a Z-
24 R relationship to obtain the rain rate from the radar.

25 The results obtained indicate that this set of techniques has potential for ra-
26 dar quality control in addition with other methodologies designed to improve the
27 quality of weather radar precipitation estimates.

28

29

30

31

32 **Keywords:** Doppler Weather Radar; Data Quality Control; Quantitative Precipitation Es-
33 timation.

34 1. Introduction

35 As precipitation has such an important influence on our society, a dense
36 infrastructure to measure rain has been deployed worldwide. The rain measurement and
37 forecast is a recurring problem that has involved many scientists. Weather radar rainfall
38 estimation had a great progress recently, complementing traditional raingauge networks
39 and becoming the most useful tool to measure precipitation. In recent years, due in part to
40 the increasing computing power and the technological development in the field of remote
41 sensing, much more precise and reliable algorithms to establish a radar based
42 Quantitative Precipitation Estimation (QPE) have been implemented. On the other hand,
43 experiments and simulations have been developed in order to quantify the associated
44 error in radar rain detection, conceptual changes have been performed in the radar
45 precipitation observation and synergies between various platforms have been developed
46 in order to correct inherent errors in the weather radar observations.

47 The weather radar is an electronic device capable of transmitting an electromagnetic
48 signal to the atmosphere. If this signal intercepts some target with different refractive
49 properties than the air, scattering occurs and a fraction of this energy (emitted by the
50 radar) is backscattered towards the radar (as an echo) and then the radar can relate these
51 echoes with the characteristics and location of the target.

52 The wavelength at which the weather radar operates ensures that the effective radius
53 of the particles interacting with the signal emitted by the radar is no greater than
54 about one order of magnitude less than hydrometeors (precipitation particles), so measurements
55 are made under the so-called Rayleigh conditions. The amount of this backscat-

56 tered energy is proportional to the six power of the drop diameter. Using the radar equa-
57 tion, this energy can be converted into a measure of reflectivity.

58 *1.1 Radar geometry*

59 The weather radar scans the atmosphere setting an elevation (polar) angle and
60 then rotate 360° degrees in the azimuthal angle. When the radar ends this sweep, the pro-
61 cess is repeated with the next elevation angle. The direction of the targets is determined
62 by means of the antenna's azimuth (ϕ) and elevation (θ) at the time of observation. The
63 distance (r) at which the targets are obtained by a clock system that counts the elapsed
64 time (t) between transmission of a pulse and echo reception, $r = ct/2$, where c is the
65 speed of light in the atmosphere. The maximum distance for which the targets are located
66 correctly is $R_{max} = \frac{c}{2PRF}$, where the PRF is the Pulse Repetition Frequency. When
67 standard refraction applies, the target height can be determined by the following equa-
68 tion:

$$69 H = \sqrt{r^2 + R'^2 + 2rR' \sin(\theta)} - R' + H_0 , \quad (1)$$

70 where (r) is the target distance form the radar, (θ) is the elevation angle, H_0 is the
71 height of the radar antenna, and $R' = 4/3R$, being R the Earth's radius.

72
73 Since the propagation conditions can affect significantly the radar beam path, the
74 beam height (H) depends on the vertical profiles of temperature and humidity.

75 The raw radar data consists of all radar beams signed by their elevation and azi-
76 muth angle (see [Figure 1](#)). Each of these radar sweeps at a constant elevation angle is
77 called Plan Position Indicator (PPI). The PPI can be depicted by a circle with center at the

78 radar site and radius equal to the radar range (≈ 240 km is usual range), where each point
79 inside this circle has a spatial resolution (of the order of 1 km^2).

80 *1.2 Radar equation*

81 Raindrops, snowflakes and condensed water droplets in clouds are examples of
82 radar targets. The hydrometeors are characterized by the presence of many elements,
83 which interact with the radar pulse, dispersing its energy. The volume containing these
84 particles is called radar volume and is determined by the beam width and pulse duration
85 (for theoretical computations, we use 1 m^3 volume)

86 The average power received by the radar (\bar{P}_r), originated at some radar resolution
87 volume composed by spherical particles that fulfill the Rayleigh approximation, is given
88 by equation 2

$$89 \quad \bar{P}_r = P_t \frac{G^2 \pi 2}{(4\pi)^3 r^4 \lambda^2} 64 \frac{(\pi)^5}{\lambda^4} |\mathbf{K}^2| \sum D^6 , \quad (2)$$

90 know as radar equation, as a function of the radar parameters (the antenna gain G ,
91 the power emitted by the radar P_t , the wavelength λ , the target distance from the radar r
92 and two factors that depend on the targets: the complex index of refraction \mathbf{K} and the
93 cross section D .

94 At a US standard temperature range, the \mathbf{K}^2 value is about 0.93 for liquid water
95 and 0.21 for ice. Therefore, an ice spherical target backscatters less power (6.5 dB) than a
96 same size liquid water sphere.

97 Because the radar equation is valid only in the Rayleigh region (target diameter \leq
98 0.1λ , where λ is the radar wavelength), the radar ability to relate unequivocally these tar-
99 gets with their backscattered energy are conditioned to the radar wavelength and the

100 target size. For very large hydrometeors (like hail) the backscatter energy does not vary
101 proportionally to the particle size. On the other hand, tiny particles like cloud droplets
102 will produce any detectable backscatter energy for C and S-band radars.

103 The summation of all the backscattering cross sections ($\sum D^6$) induces a quantity
104 called reflectivity (Z), defined as:

105
$$Z = \sum_v D^6 = \int_0^\infty N(D)D^6 dD , \quad (3)$$

106 where $\sum_v D^6$ indicates the summation per volume unit, dD stands for the number
107 of targets with diameter between dD and $D + dD$ per volume unit, and $N(D)$ is the drop
108 size distribution (DSD). Z is measured in $\text{mm}^6 \text{m}^{-3}$, representing the scattering cross sec-
109 tion of all hydrometeors within one cubic meter. Because of the large range of reflectivi-
110 ties, the following logarithmic units are used (decibels of Z or dBZ):

111
$$dBZ = 10 \log Z . \quad (4)$$

112 Almost all the weather services around the world display the radar echoes using
113 dBZ as a unit.

114 The radar equation (2) can be redefined in terms of (3) as:

115
$$\bar{P}_r = \frac{\pi^3 C}{2^{10} \ln(2)} \left[\frac{P_t G^2 \theta^2}{\lambda^2} \right] \left[|K^2| \frac{Z}{r^2} \right] . \quad (5)$$

116 This equation is the most useful representation of the radar equation, having sepa-
117 rate terms for the radar parameters and target (first and second terms in brackets, respec-
118 tively). See [Doviak and Zrnic \(1993\)](#) and [Meischner \(2005\)](#) for more details on this equa-
119 tion.

120 *1.3 Radar quantitative precipitation estimation (QPE)*

121 The QPE was born from the need to transform the radar reflectivity (Z) into rain
122 rate, and thus many techniques have been developed for this purpose. All these tech-
123 niques are oriented to improving the radar observations.

124 A classical example of this are the $Z-R$ relationships, which compute the rain rate
125 using a power-law $Z = A R^b$, where A and b are constants, R is the rain rate in mm h^{-1}
126 and Z is the radar reflectivity, as proposed by radar pioneers [Marshall and Palmer \(1948\)](#).
127 Note that there are hundreds of $Z-R$ relations in the literature.

128 The largest problem in applying $Z-R$ relationships are the errors associated with
129 the measurement of the reflectivity, (e.g. wet snowflakes produce a larger echo than wa-
130 ter drops, etc). Another factor affecting the $Z-R$ relationships is related to the fact that
131 the reflectivity (Z) is more sensitive to the drop diameter (six-power) than to the drop
132 density, while the rain rate depends on the third-power of the drop diameter. Other im-
133 portant problems are the mixed phase precipitation, the interception of the radar beam
134 with the terrain, or the fact that radar observations are made at a given height above
135 ground (which increases with the distance to radar site) and not close to the ground.

136 As we have seen in the previous example, the main challenge of the QPE is to
137 solve the inherent radar inaccuracies and to propose solutions to these. According to
138 [Meischner et al. \(1997\)](#) and [Joss and Waldvogel \(1990\)](#), this sources of uncertainty can
139 be grouped into:

140 • Radar calibration;
141 • Interception of the radar beam with the orography and non-meteorological tar-
142 gets;

- 143 • Signal attenuation due to precipitation;
144 • Propagation conditions effect;
145 • Errors related to the Z–R relationship.

146 We will give now a sketch of the techniques used to correct these errors.

147 The radar calibration is related to the factors appearing in the second term of
148 equation 2 and with inaccuracies in the radar pointing system. Notice that 1 dBZ dBZ
149 error corresponds to 15% error in R . The work of [Joss et al. \(1996\)](#), based on results ob-
150 tained in Germany and Switzerland gives a good review on radar calibration. Some cali-
151 bration processes involve spherical metal targets which are used as radar pulse reflectors.
152 The works of [Manz et al. \(2000\)](#) and [Meischner \(2005\)](#) give an overview of the calibra-
153 tion techniques used by the Northern Europe Radar Network NORDRAD.

154 The interception of the radar beam with the orography occurs when there is an ob-
155 stacle (usually a cliff) that interferes with the radar beam causing a beam blocking. The
156 work of [Bech et al. \(2007b\)](#) and [Bech et al. \(2003b\)](#) quantifies and identifies echoes
157 caused by this blockage.

158 The signal attenuation is caused because the targets absorb part of the radar ener-
159 gy. Attenuation depends strongly on the radar frequency (high frequency implies more
160 attenuation, *i.e.* is more important in X-band than C-band, and is negligible in S-band ra-
161 dars). The big storms generally cause a shadow behind them where precipitation is un-
162 derestimated by the radar. The work of [Berenguer et al. \(2002\)](#) explores this topic.

163 Deviations from the standard temperature and humidity vertical profile modify the
164 radar beam path causing superrefraction. Hereby the beam, is bent towards the Earth's
165 surface causing clutter echoes (spurious echoes). This condition is known as Anomalous

166 Propagation (AP). This phenomenon was also studied by [Bech et al. \(2002\)](#), [Steiner and](#)
167 [Smith \(2002\)](#), [Dixon \(2007\)](#) and [Fornasiero et al. \(2005\)](#). Another possible condition aso-
168 ciated with the departures from the normal temperature and humidity is the subrefraction,
169 where the radar beam is bent towards the space causing a shorter radar range.

170 The errors due to the use of an inappropriate $Z-R$ relation were studied by [Joss](#)
171 [and Waldvogel \(1990\)](#). The $Z-R$ relationship associated problems were discussed above
172 in this section.

173 *1.4 Non meteorological echoes*

174 Since the first radar applications echoes coming from fixed targets contribute to
175 the received signal, these echoes are called clutter and can be classified (after [Bøvith](#)
176 [\(2008\)](#)) according to their origin into the following categories:

- 177 1 Land clutter from (a) mountains/earth surface or (b) buildings/windmills, etc;
- 178 2 Sea clutter from (a) sea surface or (b) ships;
- 179 3 Airborne clutter from (a) biological targets (birds/insects) or (b) airplanes;
- 180 4 Interference clutter from (a) the sun or (b) transmitting antennas.

181

182 [Figure 2](#) illustrates the typical sources of clutter, showing their diversity and that, while
183 some are static objects, many of them are in motion, as is the sea surface, the insects and
184 the sunlight beams.

185 The main factors that can cause clutter are the following. *Beam blocking* causes
186 static echoes due to the radar beam interaction with buildings or towers that are close to
187 the radar site or due to the topography. This type of clutter is typical in mountainous are-
188 as.

189 *Anomalous propagation* which can generate land and sea clutter. The big differ-
190 ence between this factor and the previous one is that, in this case, the echoes caused by
191 the AP can appear or disappear depending on the propagation conditions and can affect
192 much larger areas.

193 It is important that the removal and identification clutter methods do not eliminate
194 the echoes that come from hydrometeors. The work of [Meischner et al. 1997](#) gives a good
195 review of the techniques used for this matter. The strategies used to remove these echoes
196 can be divided into six groups according to [Joss \(1995\)](#) and [Magaldi et al. \(2009\)](#).

197 1) Map: It allows to identify the clutter by its morphology using clear air observa-
198 tions as a reference.

199 2) Doppler: It filters the echoes of the static clutters, *i.e* those whose radial ve-
200 locity is zero.

201 3) Statistical: Using beam information, the clutter is characterized.

202 4) Interpolation: Using vertically or horizontally adjacent information, the zones
203 affected by clutter are identified.

204 5) Polarization: The polarimetric radars recognize the clutter by its polarization
205 signatures.

206 6) Multisource: Using information from other sources, the AP echoes can be iden-
207 tified.

208

209 2. Environment of study

210 Greater Mexico City is the metropolitan area of (conurbation around) Mexico City
211 (MCMA) occupies an area of 7,854 km², of which 1,500 km² are fully urbanized (see
212 [Figure 3](#)). With just over 21 million habitants, it is among the most populated cities in the

213 world. The MCMA includes 76 municipalities in the States of Mexico, Hidalgo and Mex-
214 ico City (CDMX), which has been reported in 2015 to have a population density of 6,000
215 people / km² and to have a total population of almost 9 million, is the capital city, and the
216 economic and political center of the country.

217 The CDMX is located in the Valley of Mexico, placed in the Trans-
218 Mexican Volcanic Belt. The city has a minimum altitude of 2,200 m.a.s.l and the moun-
219 tains and volcanoes that surround the city reach elevations of over 5,000 meters. The Val-
220 ley of Mexico has no natural outlet for the waters that flow from the mountains, making
221 the city vulnerable to flooding. This, together with the fact that the city center was built
222 on a lake, which causes the city to sink several centimeters a year, rebounds on the city
223 losing its discharge capacity, which forces the use of pumps to discharge the wastewater
224 and stormwater out the Valley.

225 *2.1 Rain patterns at Valle de México*

226 Recent works have analyzed the precipitation patterns in the Valley of Mexico,
227 among which the works of [Caetano et al. 2012](#) and [Arnaud et al. 2002](#) stand out, where
228 the precipitation patterns in the valley are described, pointing out a maximum during the
229 month of June (in this region the rainy season starts in late May and finishes early Octo-
230 ber). The mean annual rainfall is approximately 600 mm at 2240 m and 1100 mm at the
231 mountains, the intense rainfall events can reach 172 mm in 24 hours ([Arnaud et al. 2002](#)).

232 The previous characteristics imply that the Valley of Mexico wet season has a
233 monsoon regimen and a strong influence of the orography in the rain distribution. This
234 fact was reported by [Carrera-Hernández 2007](#) who used interpolation methods to recon-
235 struct the precipitation field in the Valley of Mexico from 200 weather stations, showing

236 the correlation of the terrain height over the Valley of Mexico with the precipitation in-
237 tensity.

238 On the other hand, the work of [Ochoa et al. 2015](#), shows the modification of the
239 precipitation patterns due to the pollution of the Valley of Mexico, indicating that micro-
240 physical processes have the potential to shift the timing of precipitation to earlier times.

241 *2.2 Cerro Catedral radar*

242 The radar data were collected from the Cerro Catedral (CC) C-band Doppler sys-
243 tem, located near Mexico City (19.550 N, 99.520 W), which belongs to the National
244 Weather Service of Mexico (SMM) radar network (see [Figure 3](#)). This radar was installed
245 in the beginning of 90s, the system was upgraded in December 2007, when the original
246 Ericsson weather radar UBS 103 04 was upgraded using the Sigmet/Vaisala technology,
247 signal processor RVP8, radar control processor RCP8, RF to IF receiver with calibrated
248 noise source and a solid state transmitter and modulator model TR1061. From the origi-
249 nal Ericsson radar remains the Ericsson pedestal and antenna with the diameter of 4.2m
250 (beamwidth < 1 deg.), the radome, part of waveguides, rotary joints and the waveguide
251 dehydrator-compressor. [Table 1](#) provides a comprehensive information of this radar.
252 The Cerro Cathedral radar performs 3 plan position indicator (PPI) scanning modes every
253 15 minutes:

- 254 • Surveillance scan at -0.5 degrees elevation at 300 km range,
255 • Volume scan 0 to 10 degrees at 240 km range,
256 • VAD volume scan – 3 higher elevation sweeps at short range.

257 In the present study, the surveillance scan (PPI) data from January 1st 2015 to
258 December 31st 2015 were used, corresponding to a -0.5° antenna elevation angle, 300 km

259 of maximum range and 1 km of radial resolution (see Table 1 for more details on the ra-
260 dar configuration).

261 3. Methodology for clutter discrimination

262 3.1 Cerro Catedral radar propagation model

263 The altitude difference from Mexico City is approximately 1.5 km. [Magaldi 2017](#)
264 used a propagation model with an effective Earth radius of $\frac{4}{3} * r_e$, (where r_e is the
265 Earth radius) and normal propagation conditions (VRG of -40 $\partial N / \partial z$) to find the beam
266 height for the Cerro Catedral radar over CDMX (see [Figure 4 \(b\)](#)), showing that, for a
267 0.5 degree elevation, the radar beam is at 3 km over the CDMX. Therefore, the use of
268 negative elevations (see [Figure 4 \(a\)](#)) is mandatory to measure hydrometeorological tar-
269 gets close to the ground level at Valley of Mexico. However, the height of the radar beam
270 over the CDMX makes it difficult for the radar to properly measure the precipitation
271 caused by stratiform systems.

272 3.2 Rain patterns in the Valley of México

273 We present here the precipitation pattern for the year 2015 obtained from the sur-
274 face automatic meteorological stations network of the Atmospheric Monitoring System
275 (SIMAT), which belongs to the CDMX Ministry of Environment distributed throughout
276 the Valley of Mexico. This network is composed of a total of 26 stations ([Figure 3](#)).

277 The data management and the graphics generated in this section were made with
278 the library aire.zmvm ([Del Valle, 2018](#))

279 From these data, we calculate the weekly accumulated rain in the Valley of Mexi-
280 co for the period January 1st 2013 to December 31st 2016. [Figure 5](#) shows a well defined
281 wet season, also depicted a few weeks where the cumulative rainfall exceeds 150 mm, a
282 According to [Hyndman, R. J. and Grunwald \(2002\)](#) a Generalized Additive Model
283 (GAM) was applied over the 26 stations with the objective find trends and smooth the
284 accumulated rain time series (blue line at [figure 5](#)), the GAM model suggest the absence
285 of any tendency (increase or decrease) at the precipitation time series.

286 The 2015 weekly accumulated precipitation indicates that this year is a good can-
287 didate to measure the capabilities of the weather radar as it shows a well-defined rainy
288 season with several events of intense precipitation plus a spatial distribution of precipita-
289 tion that does not show extremely large bias among regions, as shown in Figures 5 and 6.

290 *3.2 Clutter suppression techniques.*

291 Due to the complex orography of the Valley of Mexico and the fact that the personnel of
292 the SMN control the processing of Cerro Catedral radar data, it was decided to apply an
293 algorithm that was able to handle these situations: the Gabella algorithm ([Gabella, M.,](#)
294 [and R. Notarpietro, 2002](#)).

295 The Gabella algorithm is based on the premise that the non-hydrometeorological
296 targets (non-stationary and stationary) decorrelate rapidly in space and are spatially het-
297 erogeneous to a great degree. The signatures of these echoes may be identified in the re-
298 flectivity data, because their spatial variability is larger than the hydrometeorological
299 echoes. The Gabella algorithm uses the horizontal spatial variability of the radar reflectiv-
300 ity field as proxy to identify the spurious echoes. The algorithm has two parts: one part
301 consists of a spatial-proximity filter applied to each pixel in the radar image in order to

302 eliminate the pixels that are weakly spatially correlated to their neighbors. The second
303 part is a test of compactness due to the larger spatial continuity of the hydrometeorologi-
304 cal targets than non-hydrometeorological, designed to identify adjacent pixels of not null
305 intensity, grouping the pixels in a 8 by 8 sub grid and setting a ratio of the number of
306 pixels in the sub grid and the pixels in the sub grid boundary.

307 *3.3 Attenuation correction*

308 A basic forward gate-by-gate correction was applied to the Cerro Catedral radar
309 data. This technique, introduced by Hitschfeld and Bordan (Hitschfeld, W. and Bor-
310 dan, J. 1954), recursively corrects the reflectivity in each radar range using total path-
311 integrated attenuation (PIA), which is retrieved by accumulating the specific attenua-
312 tion of each gate over the entire propagation path, then the corrected reflectivity is com-
313 puted for each gate by adding the PIA of the gate to the reflectivity measured in that
314 gate.

315 *3.3 Data flow*

316 The strategy to follow in this work is as follows; the raw radar data is processed and ex-
317 ported with the Iris software, then for each radar scan the clutter detection is performed,
318 then the attenuation correction is made and finally the Marshall Pallmer (Z-R) equation
319 is applied with the following parameters ($A=220$, $b=1.6$). Finally, the rain accumulation
320 (mm) is computed from the rain intensity (mm/h). Each stage described above is stored in
321 order to perform the annual accumulation of these fields.

322

323 4. Results and discussion

324 The two methods described in the previous section were implemented to correct
325 observations of the SMM Cerro Catredal weather radar. One year radar accumulation
326 where selected to illustrate this methodology, the [Figure 7](#) shows the raw radar data ac-
327 cumulation. From this figure, it is easy to observe that the CC radar presents artifacts due
328 to:

- 329 • Electromagnetic interference;
- 330 • Birds and insects detection;
- 331 • Jamming;
- 332 • Ground clutter due to non-meteorological targets;
- 333 • Signal noise;
- 334 • Attenuation;
- 335 • Sun interference.

336 By analyzing [Figure 7](#), it can be deduced that the beams that leave the radar and propa-
337 gate eastwards are due to electromagnetic interference or the sun's rays, the purple spots
338 observed that surround the radar (approximately 100 km) are due to the ground clutter,
339 the black spots that are observed very close to the radar are due to the detection of insects
340 or birds by radar. On the other hand, the rays that leave the radar towards the Northwest
341 and Southwest and that have a lower intensity than the rays originated by electromagnetic
342 interference are surely occasioned by jamming (presence of intensive nearby transmitters)

343 After applying the Gabella algorithm, a map with the distribution of the CC radar
344 clutters was generated (Figure 8), where it can be seen that there is a large accumulation

345 of these artifacts close to the radar (detection of birds and insects) and in the south-
346 southwest area of the radar, which coincides with the block map shown in Figure 4.

347 On the other hand, comparing Figures 7 and 8, it can be deduced that, in the area
348 comprised by the large black spots on Figure 7 (low accumulation), no clutter is observed,
349 which suggests that this region is affected by attenuation. On the other hand, Figure 8 de-
350 pictis a beam in the Northwest direction, with a low concentration of clutter, while in Fig-
351 ure 7 it has a large accumulation, probably because this beam is due to electromagnetic
352 interference.

353 After applying the Gabella filter, an attenuation correction was applied to the CC
354 radar data. Figure 9 shows the accumulation of the corrected and filtered data, which,
355 compered to Figure 7, it stands out that most of the artifacts have disappeared, particula-
356 rly those caused by electromagnetic interference and the ground clutter. It can also be seen
357 that the attenuation correction improved the radar observations in the Southwest area of
358 the radar (large black spots on Figure 7).

359 The accumulation of precipitation shows that, although the radar suffers from in-
360 tense attenuation, its operation is correct in the Valley of Mexico (50 -100 km East direc-
361 tion), where we can see that precipitation reaches 400 mm in the lower areas of the valley
362 and 650 mm in the mountainous (South) areas of the valley, as shown in Figure 10, which
363 coincides qualitatively with the results of Caetano's work.

364

365 5. Summary and conclusions

366 A methodology to remove non-precipitating echoes in radar images by using the
367 Gabella algorithm and an attenuation correction procedure has been presented and dis-
368 cussed.

369 The results indicate that it is possible to reconstruct the precipitation field of the
370 Mexico valley using the CC radar. The applied technique reveals that the attenuation and
371 the ground clutter are the main CC radar problems and that surely their data need to be
372 calibrated.

373 One year of radar data (year 2015) was chosen as representative of the wet and
374 dry seasons at the Valley of Mexico with concurrent of extreme precipitation events. In
375 total, there were 30544 radar scenes examined to illustrate the overall performance of the
376 methodologies here considered. Further efforts will be devoted to verify in more detail
377 and with larger data sets (20 years) the methodology presented to characterize the behav-
378 ior of these algorithms in order to create the rain climatology over the Valley of Mexico.
379 The further work will include considering new approaches to improve the data quality of
380 CC radar. For example, following the works of Magaldi et al. (2009) where satellite ob-
381 servation are incorporated in order to eliminate radar spurious echoes and Ośródka et al.
382 (2014) who built data quality algorithms on 3D radar reflectivity volume data.

383 Although the results reported here confirm the potential of this set of techniques,
384 the complementary use of other algorithms designed to resolve the lack of detection over
385 the stratiform rain should be considered in order to improve the radar precipitation esti-
386 mates.

387

388

389

390

391

392

393

394

395

396

397

398

399

400

401

402

403

404

405

406

407

408

409

410

411

412

413

414

415

416 *Acknowledgments.*

417 *The author is indebted the Meteorological Service of México for providing the radar da-*
418 *ta, special thanks to Marina Herrera (CEA - Querétaro) and Armando Rodriguez (SMN)*
419 *for kindly providing valuable comments and discussions on the vaisala-sigmet hardware*
420 *placed in México at an early stage of this work and also to the two anonymous reviewers*
421 *for their constructive criticisms that enhanced the final form of this article.*

422

423

424

425

426

427

428

429

430

431

432

433

434

435

436 References

- 437 Arnaud, P., et al., 2002. Influence of rainfall spatial variability on flood prediction.
438 Journal of Hydrology, 260 (1–4), 216–230.

439 Bech, J., B. Codina, J. Lorente, and D. Bebbington, 2002: Monthly and daily variations of
440 radar anomalous propagation conditions: How normal is “normal” propagation?
441 Conference Proceedings of the 2nd European Conference on Radar in Meteorolo-
442 gy and Hydrology (ERAD), 35–39.

443 Bech, J., B. Codina, J. Lorente, and D. Bebbington 2003: The sensitivity of single polariza-
444 tion weather radar beam blockage correction to variability in the vertical refrac-
445 tivity gradient. Journal of Atmospheric and Oceanic Technology, 20, 845–855.

446 Bech, J., U. Gjertsen, and G. Haase, 2007: Modelling weather radar beam propagation
447 and topographical blockage at northern high latitudes. Quarterly Journal of the
448 Royal Meteorological Society, 133, 1191–1204.

- 449 Berenguer, M., G. Lee, D. Sempere-Torres, and I. Zawadzki, 2002: A variational method
450 for attenuation correction of radar signal. Conference Proceedings of the Second
451 European Conference on Radar in Meteorology and Hydrology (ERAD)
452 Bøvith, T., 2008: Detection of Weather Radar Clutter. Ph.D. thesis, Technical University
453 of Denmark.
454 Caetano, E, Mendez-Antonio, B and Magaña V, 2012: Use of Radar Precipitation Esti-
455 mates in Urban Areas: A Case Study of Mexico City, Doppler Radar Observa-
456 tions, IntechOpen.
457 Carrera-Hernández, J.J., Gaskin, S.J., 2007: Spatio temporal analysis of daily
458 precipitation and temperature in the Basin of Mexico. *J. Hydrol.* 336, 231–249
459 Del Valle, D., 2018: aire.zmvm, package, available at
460 <https://github.com/diegovalle/aire.zmvm>
461 Dixon, M., 2007: Intelligent mitigation of normal propagation and anomalous propa-
462 gation clutter. Proceedings, 33rd Conference on Radar Meteorology, A. M. Socie-
463 ty, ed.
464 Doviak, R. J. and D. S. Zrnic, 1993: Doppler radar and weather observations. Academic
465 Press, 458 pp. pp.
466 Fornasiero, A., P. Alberoni, R. Amorati, L. Ferraris, and A. Taramasso, 2005: Effects of
467 propagation conditions on radar beam-ground interaction: impact on data quality.
468 Advances in Geosciences, 2, 201–208.
469 Gabella, M., and R. Notarpietro, 2002: Ground clutter characterization and elimination in
470 mountainous terrain. Proc. Second European Conf. on Radar Meteorology
471 (ERAD), Delft, Netherlands, Delft University of Technology, 305–311

- 472 Hitschfeld W and Bordan J. 1954: Errors inherent in the radar measurement of rainfall at
473 attenuating wavelengths. *J Meteorol.* 11:58–67.
- 474
- 475 Hyndman, R. J. and Grunwald, G. K., 2002: Applications: Generalized Additive
476 Modelling of Mixed Distribution Markov Models with Application to Mel-
477 bourne's Rainfall. *Australian & New Zealand Journal of Statistics*, 42: 145–158.
- 478 Joss, J., 1995: Improvement of current weather radar systems. Technical report, C. G.
479 Collier, Ed., European Commission.
- 480 Joss, J. and A. Waldvogel, 1990: Precipitation measurements and hydrology. Radar in
481 meteorology Battan memorial and 40th anniversary radar meteorology confer-
482 ence, D. Atlas (Ed.), American Meteorological Society, 577–606.
- 483 Joss, J., H. London, and J. Weisbarth, 1996: Need and verification of the accuracy for
484 hydrological radar applications. 20th Nordic Meteorology Conference, Sweden,
485 volume 8, 96.
- 486 Magaldi, A. V., J. Bech, and J. Lorente, 2009: A multisource scheme based on NWP and
487 MSG data to correct non-precipitating weather radar echoes. *Meteorology and*
488 *Atmospheric Physics*, 105, 121–132.
- 489 Magaldi, A. V, 2017: Mejora en la estimación de la precipitación en el valle de México.
490 Reunión anual de la UGM, Puerto Vallarta, México.
- 491
- 492 Manz, A., A. Smith, and P. Hardaker, 2000: Comparison of different methods of end to
493 end calibration of the U.K. weather radar network. *Physics and Chemistry of the*

- 494 Earth, Part B: Hydrology, Oceans and Atmosphere, 25, 1157–1162,
495 doi:0.1016/S1464- 1909(00)00171-4.
- 496 Marshall, J. S. and W. Palmer, 1948: The distribution of raindrops with size. Journal of
497 Meteorology, 9, 327–332.
- 498 Meischner, P., 2005: Weather radar: principles and advanced applications. Springer, 337
499 pp. pp.
- 500 Meischner, P., C. Collier, A. Illingworth, J. Joss, and W. Randeu, 1997: Advanced
501 weather radar systems in Europe- The COST-75 action. Bulletin of the American
502 Meteorological Society, 78.
- 503 Ochoa, C. A., A. I. Quintanar, G. B. Raga, and D. Baumgardner, 2015: Changes in
504 intense precipitation events in Mexico City J. Hydrometeor.,16, 1804–1820,
- 505 Ośródka, K., J. Szturc, and A. Jurczyk, 2014: Chain of data quality algorithms for 3-D
506 single-polarization radar reflectivity (RADVOL-QC system). Meteor. Appl.,21,
507 256–270.
- 508 Steiner, M. and J. A. Smith, 2002: Use of three-dimensional reflectivity structure for au-
509 tomated detection and removal of nonprecipitating echoes in radar data. Journal of
510 Atmospheric and Oceanic Technology, 19, 673–686.
- 511
- 512
- 513
- 514
- 515

516

517

518

519

520

521

522

523

524

525 **List of Figures**

526 FIG. 1. Radar scan elements. After Bøvith (2008)

527 FIG. 2. Types of weather radar clutter illustrated. After Bøvith (2008).

528 FIG. 3. Region of study showing the SMM Cerro Catredal radar location (circle) and

529 100 km coverage, The automatic rain gauge network are indicated by squares.

530 The figure also sows the urbanized area in the Valley of Mexico and the political

531 boundaries.

532 FIG. 4. Propagation model for the Cerro Catredal radar beam sowing the terrain elevation

533 (left) and the beam blockage fraction (rigth). For -0.5° (a) and 0.5° (b) PPI eleva-

534 tions

535 FIG. 5. 2003 -2016 weekly accumulated rain in the Valley of Mexico from the 26 SIMAT
536 weather stations. The black dots represent the weekly accumulated rain for each
537 station, the blue line shows the weekly smoothed (averaged) data for all the sta-
538 tions.

539 FIG. 6. 2015 weekly accumulated rain in the Valley of Mexico from the 26 SIMAT
540 weather stations. The black dots represent the weekly accumulated rain for each
541 station.

542 FIG. 7. 2015 Cerro Catedral radar raw reflectivity accumulation, for the -0.5° elevation
543 PPI and 300 km range.

544 FIG. 8. 2015 Cerro Catedral radar clutter accumulation map, for the -0.5°
545 elevation PPI and 300 km range.

546 FIG. 9. 2015 Cerro Catedral radar filtrated and corrected reflectivity accumulation, for
547 the -0.5°
548 elevation PPI and 300 km range.

549 FIG. 10. 2015 Cerro Catedral radar rain accumulation (after clutter suppression), for the
550 -0.5° elevation PPI and 300 km range.

551

552

553

554

555

556

557

558

559

560

561

562 TABLE 1. Main characteristics of the C-band Cerro Catedral radar used in this study
563

Frequency (MHz)	5624	Nyquist velocity (m/s)	4.31
Beam width (°)	0.89	Temporal resolution (min)	15
Range resolution (km)	1	Number of elevations	10
PRF (Hz)	250	Peak power (kW)	250
Pulse length (μs)	2	Maximum range (km)	300

564

565

566

567

568

569

570

571

572

573

574

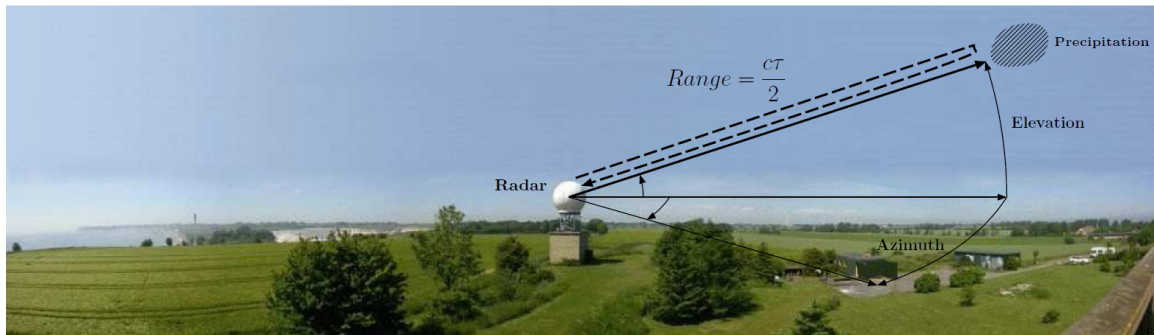
575

576

577

578

579



580 FIG. 1. Radar scan elements. After Bøvith (2008)

581

582

583

584

585

586

587

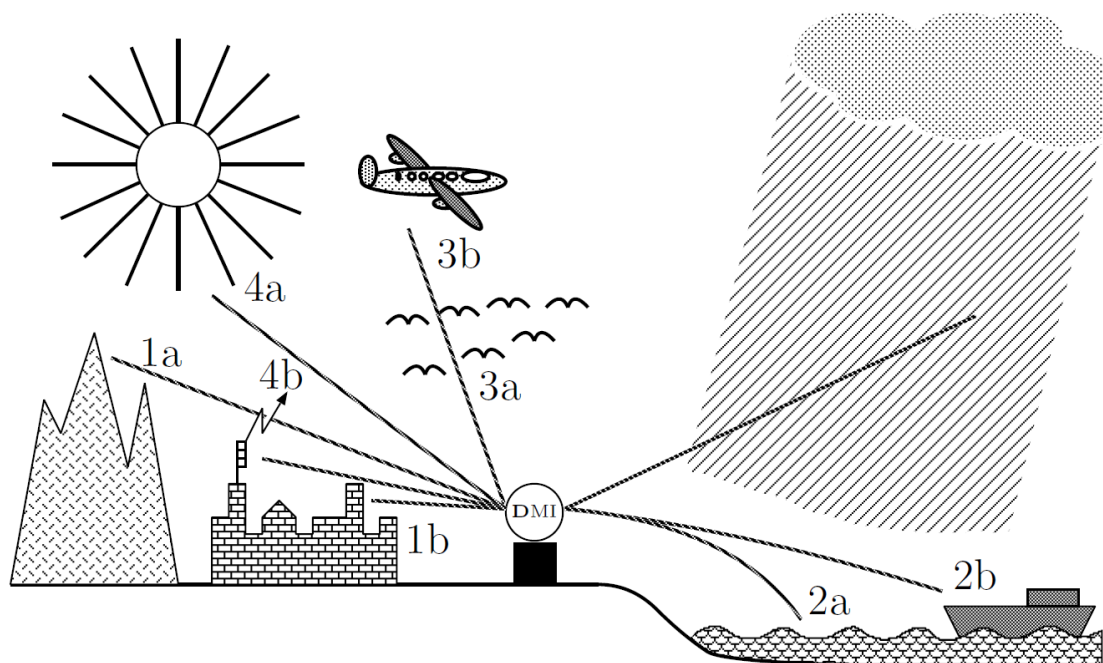
588

589

590

591

592



593

FIG. 2. Types of weather radar clutter illustrated. After Bøvith (2008).

594

595

596

597

598

599

600

601

602

603 FIG. 3. Region of study showing the SMM Cerro Catredal radar location (circle) and
604 100 km coverage, the automatic rain gauge network are indicated by squares. The
605 figure also sows the urbanized area in the Valley of Mexico and the political
606 boundaries.

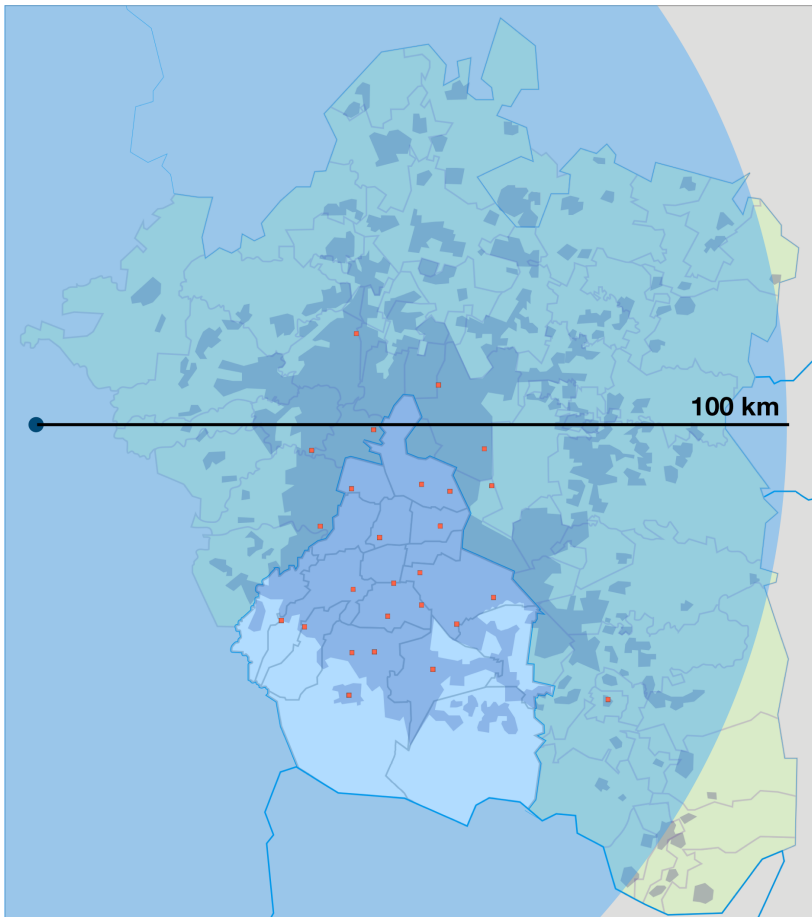
607

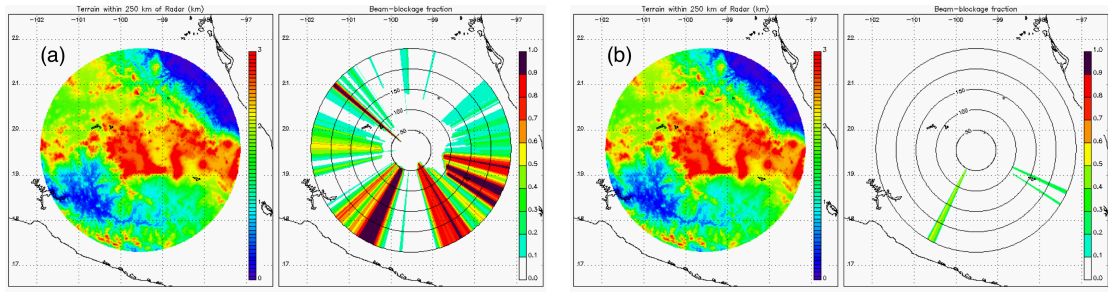
608

609

610

611





612

613 FIG. 4. Propagation model for the Cerro Catedral radar beam sowing the terrain elevation
 614 (left) and the beam blockage fraction (right). For -0.5° (a) and 0.5° (b) PPI eleva-
 615 tions

616

617

618

619

620

621

622

623

624

625

626

627

628

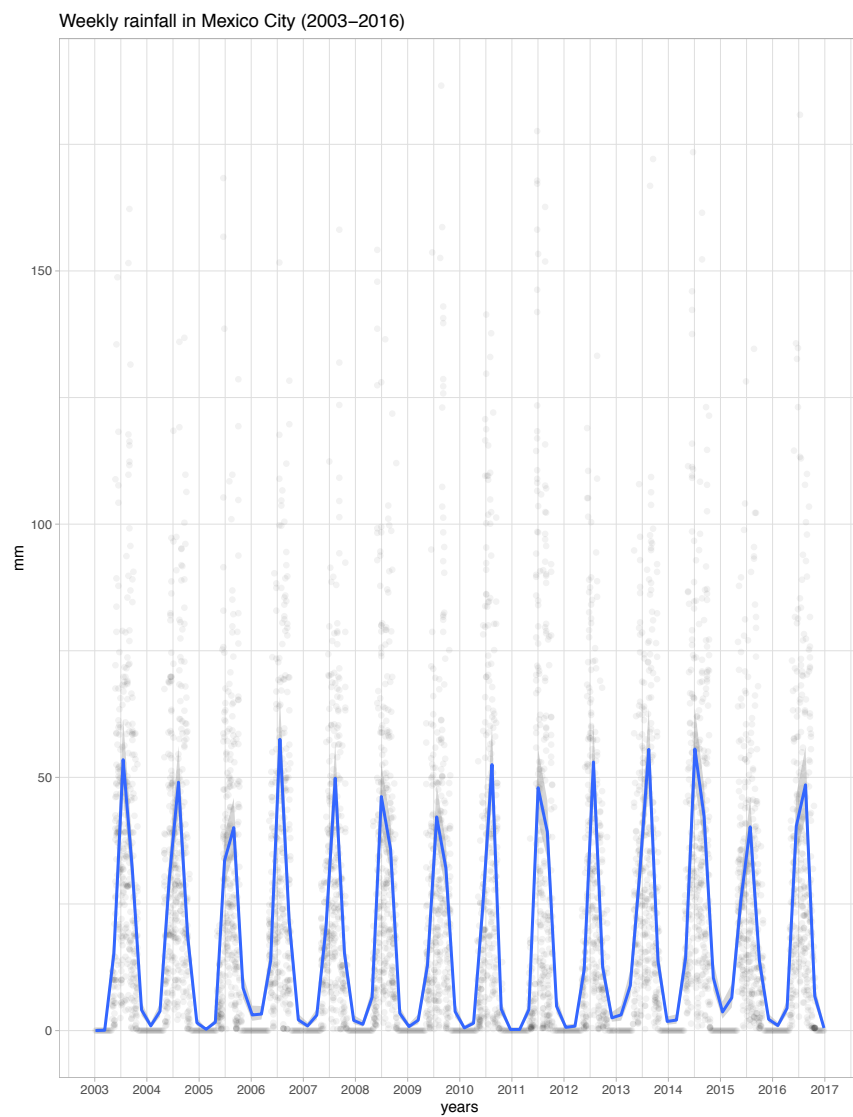
629

630

631

632

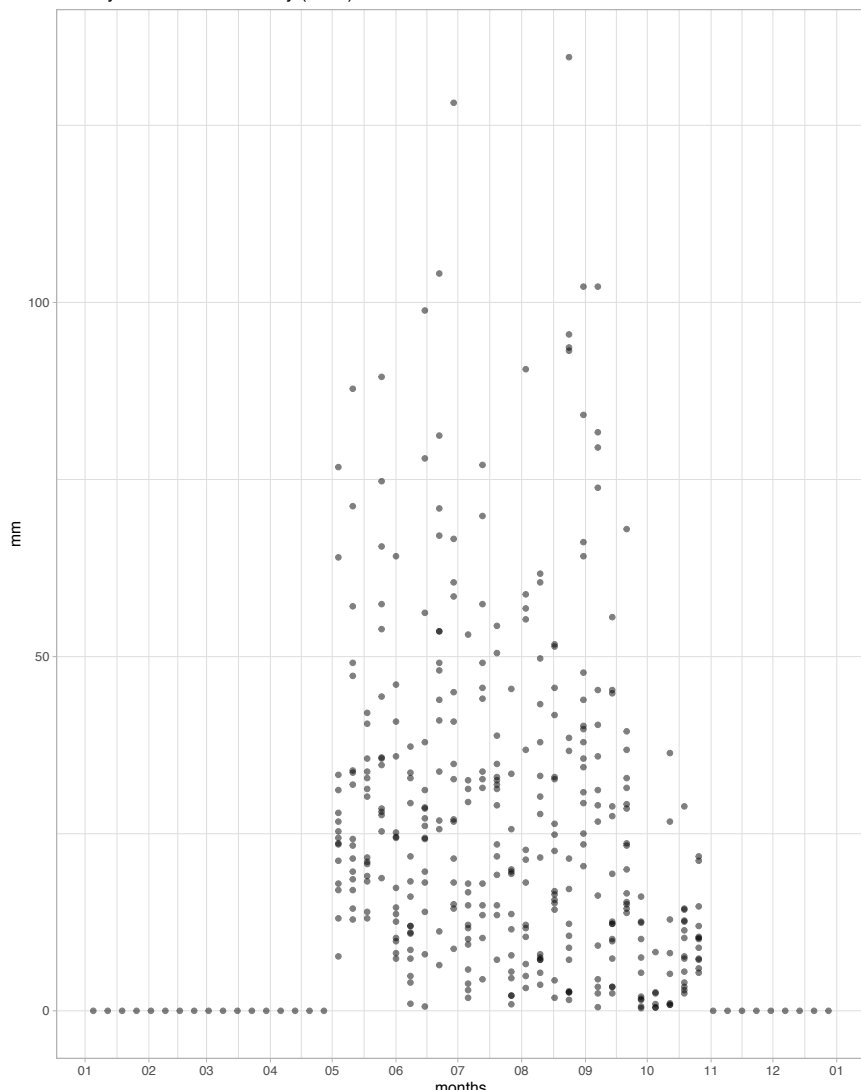
633



634

635 FIG. 5. 2003 -2016 weekly accumulated rain in the Valley of Mexico from the 26 SIMAT
636 weather stations. The black dots represent the weekly accumulated rain for each
637 station, the blue line shows the weekly smoothed (averaged) data for all the sta-
638 tions.

Weekly rainfall in Mexico City (2015)



639

640

641 FIG. 6. 2015 weekly accumulated rain in the Valley of Mexico from the 26 SIMAT

642 weather stations. The black dots represent the weekly accumulated rain for each
643 station.

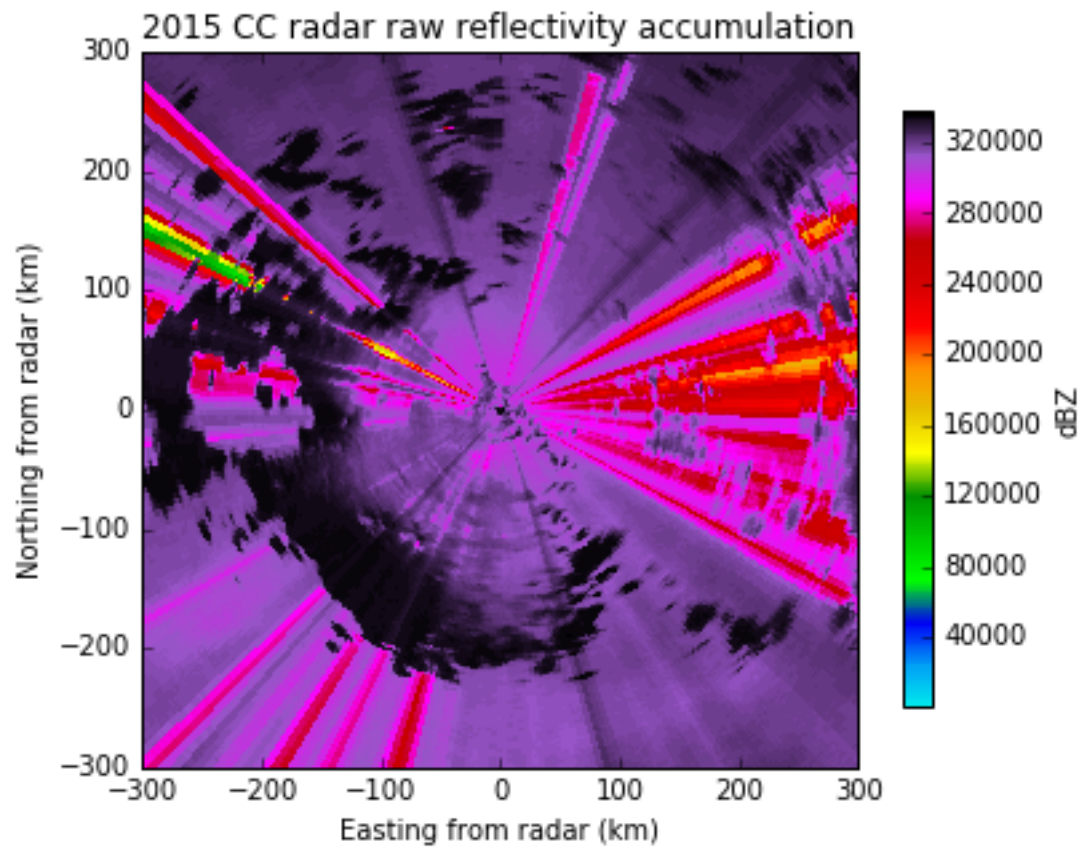
644

645

646

647

648



649

650

651 FIG. 7. 2015 Cerro Catedral radar raw reflectivity accumulation, for the -0.5° elevation
652 PPI and 300 km range.

653

654

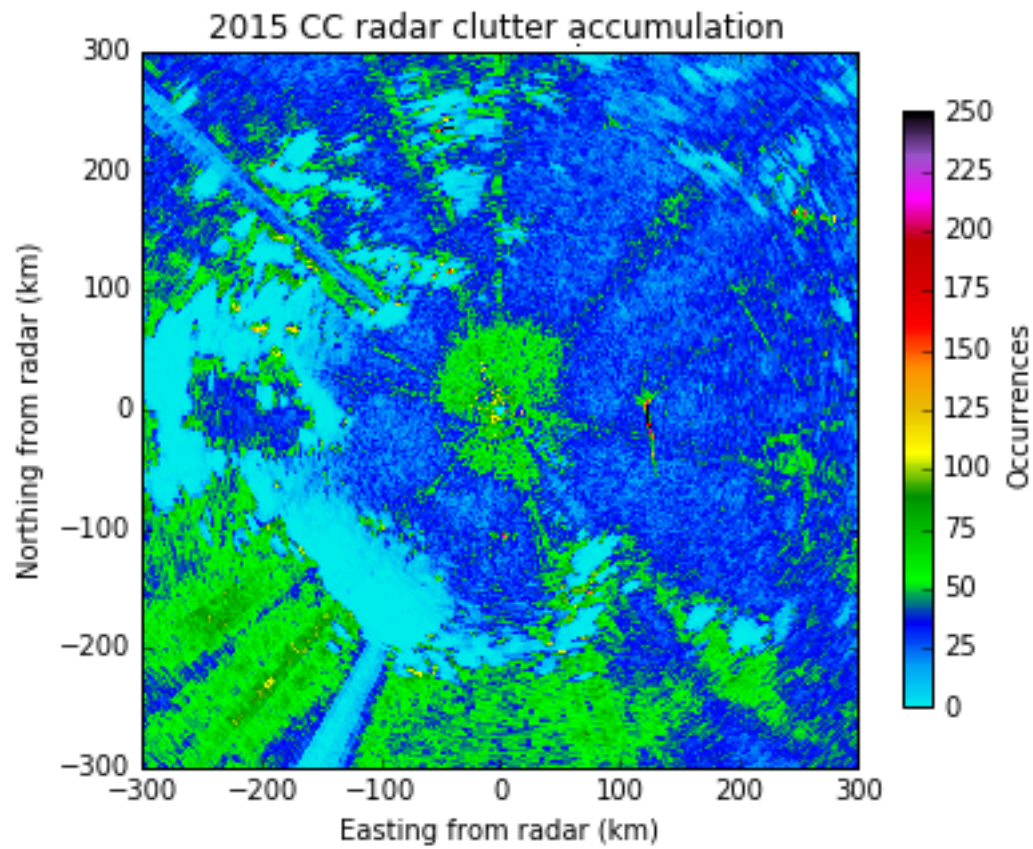
655

656

657

658

659



660

661 FIG. 8. 2015 Cerro Catedral radar clutter accumulation map, for the -0.5°
662 elevation PPI and 300 km range.

663

664

665

666

667

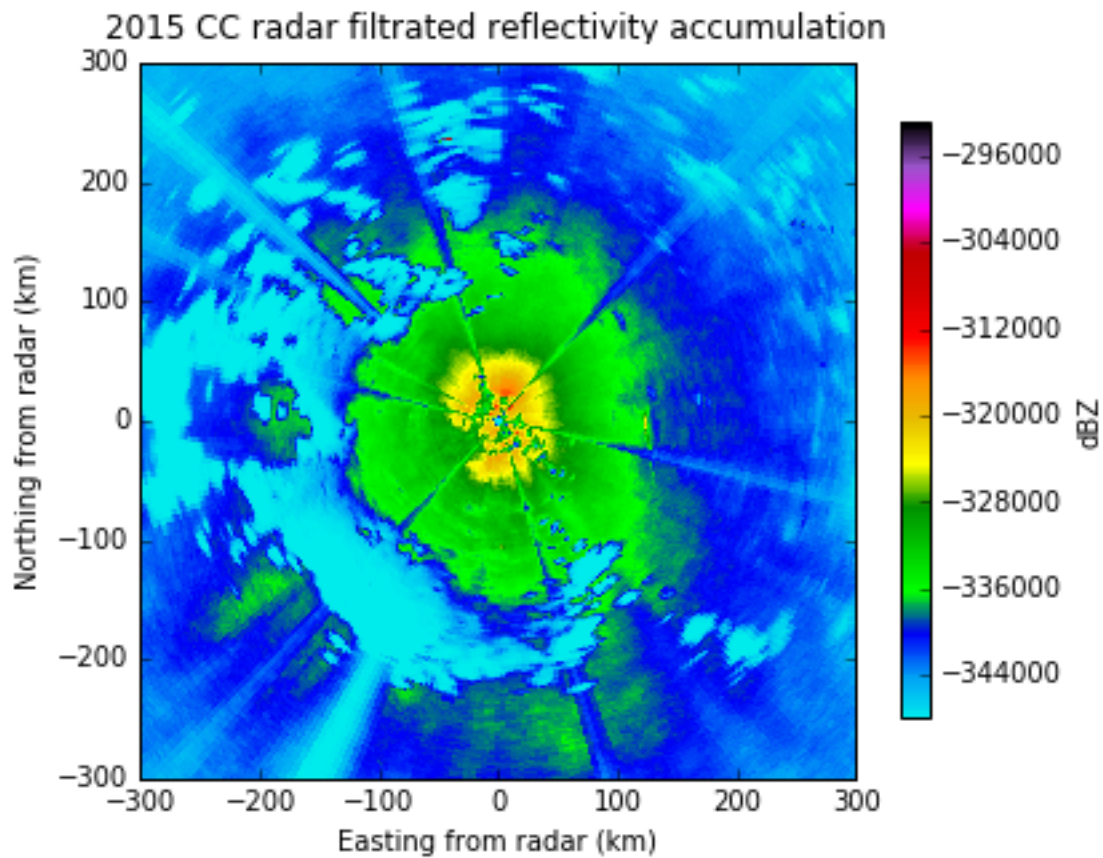
668

669

670

671

672



673

674

675 FIG. 9. 2015 Cerro Catedral radar filtrated and corrected reflectivity accumulation, for
676 the -0.5°

677 elevation PPI and 300 km range.

678

679

680

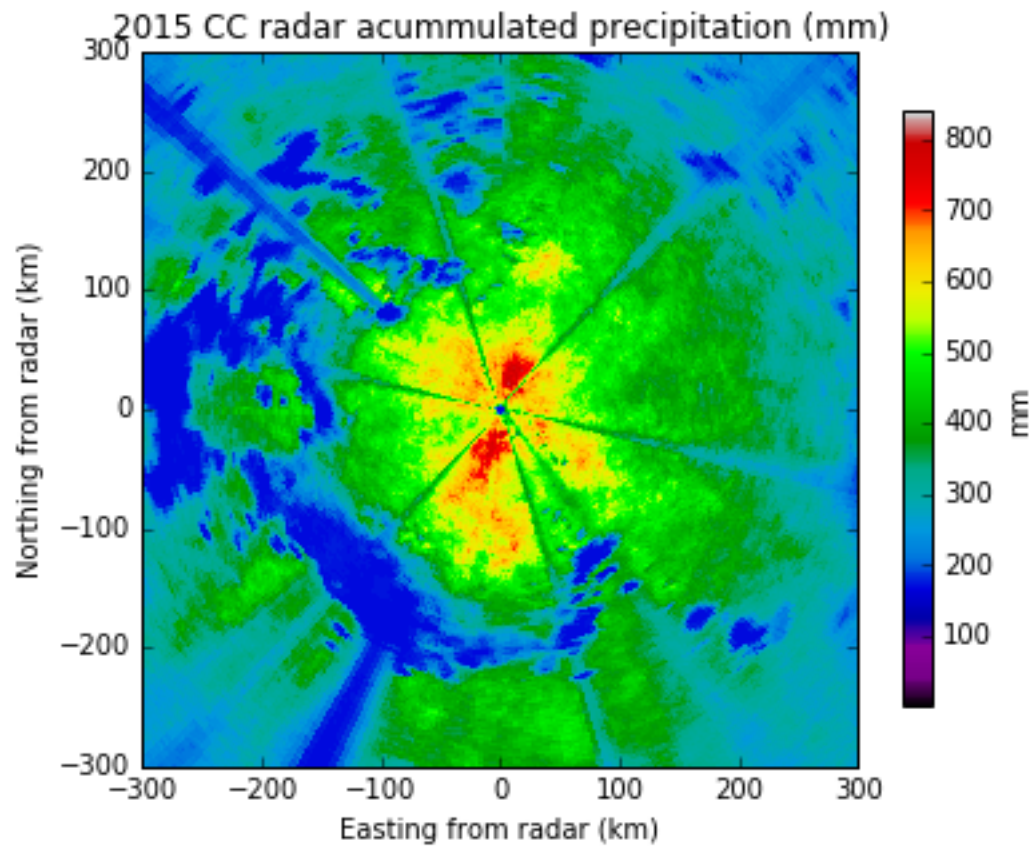
681

682

683

684

685



686

687 FIG. 10. 2015 Cerro Catedral radar rain accumulation (after clutter suppression), for the
688 -0.5° elevation PPI and 300 km range.

689

690

691

692

693

694

695

696

697

698

699

700

701